In-situ study of microstructures induced by the olivine to wadsleyite transformation at conditions of the 410 km depth discontinuity

Estelle Ledoux[1*], Matthias Krug[2], Jeffrey Gay[1], Julien Chantel[1], Nadège Hilairet[1], Maxim Bykov[3,**], Elena Bykova[3,***], Georgios Aprilis[4], Volodymyr Svitlyk[5,6], Gaston Garbarino[5], Nicolas Guignot[7], Carmen Sanchez-Valle[2], Sergio Speziale[8], and Sébastien Merkel[1]

1- Univ. Lille, CNRS, INRAE, Centrale Lille, UMR 8207 - UMET - Unité Matériaux et Transformations, F-59000 Lille, France
2- Institute for Mineralogy, University of Münster, 48149 Münster, Germany
3- Bayerisches Geoinstitut, University of Bayreuth, 95440 Bayreuth, Germany
4- Materials Physics and Technology at Extreme Conditions, Laboratory of Crystallography, Universität Bayreuth, D-95440 Bayreuth, Germany
5- ESRF, the European synchrotron, 38000 Grenoble, France
6- Helmhotz-Zentrum Dresden-Rossendorf, Institute of Resource Ecology, 01328 Dresden, Germany
7- Synchrotron SOLEIL, L'Orme des Merisiers, Saint-Aubin, F-91190 Gif-sur-Yvette, France
8- German Research Centre for Geosciences GFZ, 14473 Potsdam, Germany

Abstract

The olivine-wadsleyite transformation is believed to occur at depths of about 410 km in the Earth, producing a major seismic discontinuity in this region of the Earth's mantle. The mechanism of this phase transition controls the microstructures of the newly-nucleated wadsleyite, the major phase of the upper part of the mantle transition zone, and thus impacts seismic observations in the region. Here, we study the microstructures produced by the olivine-wadsleyite transformation using in-situ laboratory experiments at pressures and temperatures relevant for the mantle transition zone. We transform pure

*Email: estelle.ledoux@utah.edu, Present address: Department of Geology and Geophysics, University of Utah, USA

** now at: Institut für Geowissenschaften, Goethe-Universität Frankfurt, 60438 Frankfurt am Main, Germany.

*** now at: Institute of Inorganic Chemistry, University of Cologne, 50939 Cologne, Germany.

28   olivine samples in laser-heated diamond anvil cells at pressures ranging from 12.3 to 20.2 GPa and

29   temperatures of 1400-1730 K. At different steps of the transformation we measure the orientation and

30   size distribution of individual sample grains using multigrain crystallography at synchrotron radiation

31   sources. We find that the olivine to wadsleyite transformation is incoherent at the conditions of the

32   mantle transition zone, and is probably dominated by nucleation of wadsleyite at grain boundaries of

33   the parent olivine. Thus, we expect that seismic anisotropy near 410 km would drop significantly due to

34   the randomized lattice preferred orientation of newly-nucleated wadsleyite induced by the incoherent

35   transformation.

36

37   Keywords : wadsleyite, phase transformation, multigrain crystallography, lattice preferred

38   orientation, mantle transition zone, anisotropy

INTRODUCTION

40   The 410 km depth discontinuity in the Earth lies at the interface between the upper mantle and the

41   mantle transition zone (MTZ) and plays a key role in regulating mantle flow and the distribution of

42   water in the mantle (Bercovici and Karato, 2003). It displays a sharp seismic velocity and density jump

43   (Dziewoński and Anderson, 1981), attributed to the pressure-induced phase transformation of olivine to

44   wadsleyite (e.g. Ringwood, 1991; Akaogi et al., 1989; Katsura and Ito, 1989; Ito and Katsura, 1989;

45   Helffrich and Wood, 1996; Katsura et al., 2004). The correlation between the depth of seismic

46   reflections and the pressure-temperature conditions of phase transitions in the $(Fe,Mg)_2SiO_4$ system

47   (olivine-wadsleyite, wadsleyite-ringwoodite and ringwoodite-bridgmanite) has been used to estimate

48   the temperature at mantle discontinuities and anchor deep Earth thermal profiles (e.g. Katsura et al.,

49   2004, 2009).

50   Phase transitions will also affect the microstructure of a rock and large-scale geophysical

51   observations. Incoherent transformations, i.e. transformations following no orientation relationship

52   between the parent phase and the daughter phase, will erase the microstructures of the parent rock,

53   while coherent transformations, i.e. transformations where the daughter phase grows with an

54   orientation related to the parent phase, will preserve some microstructures in the daughter rock,

55   inherited from the parent rock. In the case of the olivine-wadsleyite transition, both mechanisms have

56   been reported (e.g. Smyth et al., 2012).

57   Phase transformations in olivine will affect observations of seismic signals from the deep mantle,

58   such as anisotropy or reflections off the interface, in regions where the material is downwelling. A

59   coherent olivine-wadsleyite transition will preserve lattice preferred orientation (LPO) in the newly-

60   formed wadsleyite-rich rock below the discontinuity. In contrast, the incoherent transformation of

61   olivine into wadsleyite will erase LPO and hence anisotropy of the parent olivine-rich rock (as reported

62   in Yuan and Beghein, 2013, for instance). The effect of microstructures on the underside reflections at

63   the 410 km depth discontinuity was investigated by Saki et al. (2018), and it was shown that LPO in

64   olivine above the discontinuity would in fact affect seismic observables. Microstructures in wadsleyite

65   below the discontinuity, however, will be affected by the nature of the olivine-wadsleyite phase

66   transition and deformation of wadsleyite itself. Thus, the nature of the olivine-wadsleyite

67   transformation will play an important role in the physical properties of the Earth's mantle and their

68   monitoring by geophysical observables.

69   In addition, a phase transformation affects grain sizes (e.g. Rosa et al., 2016; Perrillat et al., 2013),

70   which will also affect the properties and behavior of the rocks. Rozel (2012), for instance, showed that

71   a grain size-dependent rheology dramatically affects the convection regime of telluric planets.

72   Mohiuddin et al. (2020) also showed that the direct olivine to ringwoodite transformation at low

73   temperatures induces a fine-grained ringwoodite aggregate, deforming by diffusion creep, and with a

74   substantial strength reduction and a weakening of cold subducted slabs. As such, grain size evolution

75   during phase transitions in the olivine system is important to model the mechanical behavior of the

76   mantle and the dynamics of subduction in the MTZ.

77   Studies of phase transformation microstructures in olivine were first performed on analogs, mostly

78   germanates, due to experimental limitations (e.g. Ringwood, 1958, 1962; Vaughan and Coe, 1981; Ross

79   and Navrotsky, 1987; Burnley and Green, 1989; Ringwood and Seabrook, 1962). In germanate analogs,

80   however, the α ("olivine") phase directly transforms to the γ ("ringwoodite") polymorph, with no

81   intermediate β ("wadsleyite") phase. Hence, the olivine-wadsleyite transformation microstructures

82   require studies on the $(Fe,Mg)_2SiO_4$ system itself.

83   Experiments on the olivine-wadsleyite transformation generally indicate an incoherent nucleation

84   and growth mechanism, where no relation between parent olivine and newly-formed wadsleyite is

85   observed (Brearley et al., 1992; Kerschhofer et al., 1996, 1998; Kubo et al., 1998b, 2004; Smyth et al.,

86   2012; Mohiuddin and Karato, 2018). In addition, Kerschhofer et al. (1998) have shown that incoherent

87   nucleation of wadsleyite is dominant at olivine grain boundaries in small grain (<10-20 μm)

88   aggregates, while in large crystals (0.6 mm) intracrystalline incoherent nucleation is dominant.

89   Mohiuddin and Karato (2018) also observed both of these mechanisms in San Carlos olivine

90   polycrystals of ≈25 μm grain size and proposed that the dominance of one mechanism over the other

91   also depends on the temperature and the overpressure in the sample. These two incoherent mechanisms

92   lead to slightly different microstructures. Grain boundary nucleation is expected to produce grains with

93   random shapes while intracrystalline nucleation produces lamellae-shapped wadsleyite grains

94   (Kerschhofer et al., 1996, 1998; Mohiuddin and Karato, 2018) along olivine stacking faults on planes

95   (010) (Kerschhofer et al., 1996) or {101} (Kerschhofer et al., 1998), possibly resulting in shape

96   preferred orientation of wadsleyite grains.

97   Finally, the study of Smyth et al. (2012) documented both coherent and incoherent deformation

98   mechanism. By heating and compressing a fine-grained mixture of natural olivine, silica, FeO and

99   brucite ($Mg(OH)_2$) at 13 GPa and 1400°C in a multi-anvil press, they synthesized an aggregate

100   composed of olivine, wadsleyite, clinoenstatite and a melt phase. Quenched samples were then

101   recovered for ex-situ analysis. Transmission electron microscopy studies of these samples show that

102   small lamellae of wadsleyite were present within the remaining olivine crystals with the two following

103   crystallographic relations to the host: Type I with $[001]_{ol}$ || $[010]_{wd}$ and $(100)_{ol}$ || $\{101\}_{wd}$, and Type II

104   with $[001]_{ol}$ || $[100]_{wd}$ and $(100)_{ol}$ || $\{021\}_{wd}$. Nevertheless, the authors observed a dominance of

105   incoherent grains of wadsleyite. They hence concluded that the coherent mechanisms, although active,

106   are less efficient than the incoherent nucleation of wadsleyite and should, hence, not have a significant

107   impact on the microstructure.

108   Previous studies investigating the mechanisms of olivine-wadsleyite transformation, however,

109   mostly relied on post-mortem characterization at the local scale using optical or electron microscopy

110   (Brearley et al., 1992; Kerschhofer et al., 1996, 1998; Kubo et al., 1998a, 1998b, 2004; Smyth et al.,

111   2012; Mohiuddin and Karato, 2018). Ex-situ techniques allow a very precise determination of

112   crystallographic orientations, compositions, grain boundaries, mean grain sizes, and defect structures

113   but questions remain on whether the sample microstructures are modified at the later stages of the

114   experiment, during decompression for instance, and whether orientation relationship at the local scale

115   does affect microstructures at the bulk scale, in a polycrystal. Only a few in situ results of

116   transformation-induced microstructures were reported (Wenk et al., 2004; Rosa et al., 2016; Chandler

117   et al., 2021b), but all were performed at fairly low temperatures and focus on the olivine-ringwoodite

118   direct transformation, rather than the olivine-wadsleyite transformation, which requires higher

119   temperatures.

120   In this work, we re-address the question of microstructures induced by the olivine-wadsleyite

121   transformation using in-situ measurements at high pressure and temperatures. We rely on a recently

122   developed DAC-based experimental method, multigrain crystallography (MGC; Nisr et al. (2012);

123   Zhang et al. (2019); Nisr et al. (2014); Langrand et al. (2017)), which allows in-situ measurements of

124   crystallographic structures, grain orientations and grain statistics at high pressure during processes,

125   such as deformation or phase transformation. Previous works using MGC did not succeed to maintain

126   relevant mantle temperatures (Rosa et al., 2015; Langrand et al., 2017; Zhang et al., 2019; Chandler

127   et al., 2021a, 2021b). Here, olivine both as single-crystal and polycrystal is compressed at temperatures

128   close to those of a standard geotherm using a laser-heated DAC, and transformed into the wadsleyite

129   phase. We follow the microstructures prior to, during, and after the transformation using MGC and,

130   based on these microstructures, we investigate which type of transformation occurs in olivine at the

131   pressures and temperatures of the MTZ.

METHODS

133 Samples

134   Two starting materials were used: an olivine single crystal and sintered polycrystalline olivine

135   samples. The olivine single-crystal was a fragment of natural San Carlos olivine, with dimensions of

136   ≈ 20 μm x 20 μm and polished manually to obtain a thickness of 10-15 μm. The polycrystalline

137   samples were prepared from a powder of natural San Carlos olivine, ground in a planetary mill and

138   sintered at ≈ 25 MPa and 1500 K for 40 minutes in a piston-cylinder apparatus. A piece of the sintered

139   product was then prepared for electron microscopy and characterized in a FEG JEOL JSM-7800F

140   scanning electron microscope (SEM) using the electron back-scattered diffraction (EBSD) technique.

141   This characterization shows that it is a pure olivine polycrystal with heterogeneous grain sizes, ranging

142   between less than a micron and 50 μm, and with no preferred orientation (Fig. 1.a, b). Infrared analysis

143   shows less than 3 ppm of H_2O in the olivine grains of the sintered polycrystal (Fig. 1.c). That analysis

144   was done with a Bruker Hyperion 3000 FTIR microscope coupled with a Vertex 70 spectrometer,

145   which was equipped with a simple MCT detector and a 'Focal Plan Array' detector. Once sintered, the

146   product was cut into fine slices with a precision diamond wire saw and mechanically polished to a

147   thickness of 10-15 μm. Finally, samples were cut into disks of 20 μm diameter by lasers (Fig. 1.d).

148   In both cases, samples were coated with a 150-200 nm thick platinum layer on both sides. This step

149   ensures proper absorption of the heating infra-red lasers by the sample. It is also critical to maintain

150   stable temperatures as olivine and wadsleyite have different optical absorption properties. No signal

151   from the platinum coating is seen in the diffraction images because of the very small volume fraction of

152   platinum compared to the sample. Nevertheless, temperature stability during laser heating was

153   drastically improved for samples with platinum coating. Earlier attempts with un-coated samples

154   showed jumps in temperatures of several hundreds of degrees during pressure increases or phase

155   transformations and those datasets were systematically discarded. Such large temperature oscillations

156   did not occur when using samples coated with platinum. The platinum coating is then a convenient way

157   of increasing the stability of the heating without decreasing the diffraction signal of the sample.

158   **High-temperature / high-pressure experiments**

159   To reach the high pressure and high temperature of the 410 km depth discontinuity, we use diamond

160   anvil cells (DAC) coupled with laser heating. We used diamonds with 300 μm flat tips, rhenium gaskets

161   with holes of 100–145 μm in diameter to serve as sample chambers (Fig. 1.d), and membranes to

162   control sample pressure remotely. As pressure media, we used either MgO, KCl or alumina (Table 1).

163   All three are chemically inert in an olivine-wadsleyite system at the investigated pressure-temperature

164   conditions (Shen and Lazor, 1995; Kimura et al., 2017; Zhou et al., 2020). We can rule out undesired

165   reactions in our experiments as no other phase than olivine, wadsleyite and the pressure media are

166   present in the diffraction patterns (Figure 3). In all cases, the sample and pressure media were loaded

167   under a controlled argon atmosphere into the DAC to prevent the interaction of the hygroscopic

168   pressure transmitting media with air moisture.

169   The state of the sample was followed using in-situ multigrain X-ray diffraction at the ID27

170   beamline at ESRF, the P02.2 beamline at PETRA III, and the PSICHÉ beamline at SOLEIL. In all

171   cases, olivine was compressed at ambient temperature up to pressures between 2 and 10 GPa, after

172   which we laser-heated to achieve temperatures ranging between 1400 and 1800 K. Pressure was then

173   slowly increased while maintaining a constant temperature within ± 100 K. The sample composition

174   and pressure were monitored from the 2D-diffraction patterns using the software Dioptas (Prescher and

175   Prakapenka, 2015). Sample temperatures were measured using spectral radiometry as provided by the

176   beamlines during the experiments. At several points upon compression, pressure increase was stopped

177   to collect multigrain X-ray diffraction data by rotating the DAC over $\Delta\omega\approx60°$ (depending on diamond

178   height and cell opening) and acquiring X-ray diffraction images every 0.5° rotation increment $\delta\omega$

179   (Fig. 2). At both ESRF-ID27 and PETRA-III-P02.2, laser heating was maintained during multigrain X-

180   ray diffraction data collection, using the standard laser-heating configuration at ESRF, and using a

181   device such as presented in Bykova et al. (2019) at PETRA-III. At SOLEIL-PSICHÉ the sample was

182   quenched to ambient temperature before multigrain X-ray diffraction data collection. Sample

183   recrystallization could occur during the high-temperature 3D-XRD scans. Note, however, that

184   recrystallization is most expected in deformed grains with high concentrations of internal defects (e.g.

185   Poirier and Guillopé, 1979, Urai et al., 1986), and hence parent olivine rather than the newly nucleated

186   wadsleyite grains. In-situ 3DXRD measurements at high temperature, nevertheless, offers the great

187   advantage to avoid introducing additional deviatoric stresses upon temperature quenching that could,

188   also, affect the sample (Kavner and Duffy, 2001).

189   At the P02.2 beamline at PETRA III, X-rays were set to a wavelength of 0.2903 Å and focused to

190   7.6 (horizontal) × 4.4 (vertical) μm. The sample-to-detector distance was 398.7 mm, based on the CeO2

191   calibration. Diffraction images were collected using a PerkinElmer XRD 1621 amorphous silicon flat-

192   panel detector with 2048×2048 pixels of size (Liermann et al., 2015) for 5 s. At the ID27 beamline at

193   ESRF, we used X-rays with a wavelength of 0.3738 Å, focused to 3.2 (horizontal) × 3.0 (vertical) μm.

194   The sample-to-detector distance was 245.54 mm, based on the CeO2 calibration. Diffraction images

195   were collected using a MAR165 CCD planar detector with 2048×2048 pixels of size for 6 s. At the

196   PSICHÉ beamline at SOLEIL, we used X-rays with a wavelength of 0.3738 Å focused to about 12

197 (horizontal) × 10 (vertical) μm. The sample-to-detector distance was 389.75 mm, based on the CeO2

198 calibration. Diffraction images were collected employing a PILATUS flat-panel detector with

199 1475 × 1679 pixels of 172 × 172 μm, and with an acquisition time of 5 s. Note that the study of large

200 single crystals diffraction was allowed by the PILATUS detector that can count every photon received

201 on the panel, with high peaks spread resolution and a small readout time (Eikenberry et al., 2003), and

202 can handle significantly higher peak intensity before saturation.

203   Table 1 summarizes the experiments that were performed along with the starting materials,

204 pressure-transmitting media, and sample characterization techniques. Three experiments used pure

205 polycrystalline olivine samples as starting materials: LTC_05_01 and LTC_03_02 performed on ESRF-

206 ID27 and P2_01 performed on PETRA-III-P02.2. One experiment started from an olivine single-

207 crystal, Olivine_01 performed at SOLEIL-PSICHÉ.

208 **Diffraction data processing**

209   Post-experiment, ω-rotation multigrain diffraction images were stacked to generate an average

210 diffraction image, which was then further processed using the Rietveld refinement package MAUD

211 (Lutterotti et al., 2014; Wenk et al., 2014) from which we extract the unit cell parameters of the

212 pressure medium, olivine, and wadsleyite. The pressure was then calculated using thermal equations of

213 state from the literature (Angel et al. (2018) for olivine and Katsura et al. (2009) for wadsleyite) and the

214 EosFit Calculator software (Angel et al., 2014). Pressure and temperature conditions for each

215 multigrain measurement are summarized in Table 2.

216   The sample microstructural evolution during the transformation is processed using multigrain

217 crystallography (MGC). This method consists in acquiring 2D-diffraction images at different ω rotation

218 angles. The data is then processed to i) separate the background and the diffraction signals of the

219   pressure medium from that of the larger sample grains, ii) identify individual diffraction spots of the

220   larger sample grains, and iii) determine the sample grain orientation matrices. The detailed procedure

221   has been described in Rosa et al. (2015) and used in Rosa et al. (2016) and Langrand et al. (2017). It

222   relies on open-source softwares from the FABLE-3DXRD package, available online at

223   https://github.com/FABLE-3DXRD, additional tools from the TIMEleSS project, available online at

224   https://github.com/FABLE-3DXRD/TIMEleSS, and thoroughly described in a dedicated manual at

225   http://multigrain.texture.rocks/.

226   Individual diffraction images are first cleaned to exclude high-intensity single-crystal diffraction

227   spots from the diamond anvils and subtract the background signal. Individual diffraction spots are then

228   located using a high-pass filter, as implemented in the Peaksearch algorithm (Sörensen et al., 2012).

229   The ImageD11 software (Wright, 2006) then uses the list of extracted diffraction spots and information

230   on the experimental conditions to compute a list of potential G-vectors to be assigned to the sample

231   grains. ImageD11 does not include full crystallographic information to generate the list of G-vectors

232   and hence generate Miller indices which can be extinct in a given crystal structure. We hence re-

233   evaluate the list of potential G-vectors using our TIMEleSS scripts and the full crystallographic

234   information for olivine and wadsleyite, and concentrate on g-vectors that will actually contribute to

235   diffraction. This additional step decreases the risk of error during grain indexing. At this point, each

236   observed G-vector is assigned to its observed intensity and location in orientation space (2θ, η and ω

237   angles), and potential h, k and l Miller indices.

238   The final indexing step relies on the GrainSpotter software (Schmidt, 2014), with the following

239   settings: 100 000 random grain orientation trials, tolerances of 0.08° in 2θ, 4° in η and 3° in ω to assign

240   a measured G-vector to a grain, a minimum number of 15 G-vectors per grain, and a minimum

241   completeness of 30%. This procedure is repeated a number of times (i.e. 50), removing already

242   assigned G-vectors, to improve the number of indexed grains. The final output consists of a list of

243   grains, along with their crystallographic orientation and the list of the associated diffraction spots.

244   From the results of the MGC processing, it is possible to extract a relative size for the indexed

245   grains by scaling grain volume to the intensity of their diffraction spots. Then, using the illuminated

246   volume of the sample, the number of indexed grains and their relative volumes, we can provide an

247   estimate of their actual size, as volume or mean radius. This computation is performed using a script

248   from the TIMEleSS tools.

249   The raw multigrain data, as well as the resulting lists of grains, their orientation and grain size are

250   available online at https://doi.org/10.57745/NZFWP9 (Ledoux et al., 2023).

251   **Grain orientations analysis**

252   Indexed grain orientations are shown as either pole figures (PF; for samples with very few grains,

253   e.g. Fig. 4) or inverse pole figures (IPF) of the compression direction (for samples with a large number

254   of grains, e.g. Fig. 5). Each marker in inverse pole figures represents an indexed orientation and is

255   color-coded according to calculations based on an orientation distribution function (ODF) fitted to the

256   indexing results. Markers in pole figures also represent the orientation of indexed grains but are not

257   color-coded because orientation distributions are not relevant for a low number of grains. For this step,

258   we use the open-source MTEX toolbox for MATLAB (Bachmann et al., 2010).

259   MTEX is also used to test the effect of a coherent transformation mechanism from olivine to

260   wadsleyite. For these simulations, we start from the indexed olivine grain orientations prior to the

261   transformation and compute the daughter wadsleyite orientations resulting from a strict coherent

262   transformation. We test for both orientation relationships suggested by Smyth et al. (2012): Type I with

263    $[001]_{ol} \parallel [010]_{wd}$ and $(100)_{ol} \parallel \{101\}_{wd}$, and Type II with $[001]_{ol} \parallel [100]_{wd}$ and $(100)_{ol} \parallel \{021\}_{wd}$. The

264   simulated daughter wadsleyite orientations are also plotted as IPF, using the same procedure as above.

<div align="center">

RESULTS

</div>

266 **Transformation microstructures in olivine single crystal**

267   Sample in run Olivine_01 was an olivine single crystal at 6.3 GPa and 300 K. It was laser-heated to

268   temperatures of 1700–1800 K and compressed at 1700-1800 K over 100 minutes to drive a partial

269   conversion to wadsleyite. Multigrain crystallography data was collected on the olivine single-crystal

270   prior to the pressure increase, and at 16.1 GPa and 300 K, after the partial transformation to wadsleyite

271   and quench in temperature (Fig. 4).

272   Before the transformation (Figs. 4a,b), the sample is an olivine single crystal, as shown by both the

273   diffraction pattern and the single grain orientation deduced from the multigrain crystallography

274   processing. The diffraction image shows intense and slightly deformed diffraction peaks, indicating that

275   the crystal is large and is submitted to some stress. The multigrain crystallography processing locates a

276   single grain, with an estimated equivalent radius (i.e. the radius of a sphere with an identical volume to

277   that of the grain) of 6.1 μm.

278   Later, upon compression at high temperature, (Figs. 4c,d,e, f) the sample contains both olivine and

279   wadsleyite. Olivine diffraction peaks are still intense (Fig. 4), indicating grains of larger size, but also

280   appear elongated along the diffraction rings, suggesting that the olivine portion of the sample is

281   subdividing into different orientation domains. The multigrain crystallography processing identifies 25

282   grains of olivine with a mean radius of 0.8 μm. The orientations of these grains do not show any

283   particular alignment with specific sample directions, but are different from the orientation of the

284   original single crystal, before partial transformation to wadsleyite (Fig. 4b). On the stack of all ω

285   diffraction patterns, wadsleyite appears as small diffraction peaks forming a nearly-continuous

286   diffraction ring, suggesting that wadsleyite grains are small. On a single image of the collection,

287   however, the diffraction spots of wadsleyite are distinct (Fig. 4f). The multigrain crystallography

288   processing locates 72 daughter orientations of wadsleyite, with a mean radius of 0.8 μm. Most of these

289   grains show a cluster of orientation with their [100] crystallographic axes in the vicinity of the

290   compression direction (Fig. 4e).

291   **Transformation microstructures in polycrystalline olivine**

292   Samples in runs LTC_05_01, LTC_03_02 and P2_01 were pure polycrystalline olivine. All were

293   compressed at temperatures ranging between 1400 and 1730 K and converted to wadsleyite. Figure 5

294   presents the orientations of the grains indexed by MGC in these three experiments and at different steps

295   of the transformation.

296   In experiment LTC_05_01, the transformation from olivine to wadsleyite is observed between

297   1400 K–14.9 GPa and 1730 K–18.7 GPa. Before transformation (collection s26), MGC indexes 55

298   olivine grains with a mean grain radius of 0.5 μm and no lattice preferred orientation. After the

299   transformation (collection s27), MGC locates 114 grains of wadsleyite with a mean grains radius of

300   0.6 μm. We observe significant crystal preferred orientations, with the [100] crystallographic axes of

301   wadsleyite aligned at a low angle of the compression direction.

302   In experiment LTC_03_02, the transformation from olivine to wadsleyite is observed at 1700 K and

303   between 17.0 and 18.8 GPa. Before the transformation (collection s07), MGC indexes 180 grains of

304   olivine with a mean grain radius of 0.5 μm. The olivine grain orientations form a girdle between the

305   (100) and (010) poles of the inverse pole figure. After the transformation (collection s08), 188 grains of

306   wadsleyite are indexed with a mean grain radius of 0.5 µm and a crystal preferred orientation with the

307   maximum orientation probability 30° away from (100).

308   In experiment P2_01, the transformation from olivine to wadsleyite is observed between 1550 K–

309   20.2 GPa and 1450 K–12.3 GPa. Before the transformation (collection s06), MGC indexes 84 olivine

310   grains with a mean grain radius of 1.0 µm and no crystal preferred orientations. In this experiment,

311   pressure decreased at the olivine to wadsleyite conversion, with data collected while olivine and

312   wadsleyite coexist (collection s07) leading to 83 olivine grains with a mean grain radius of 0.7 µm and

313   no crystal preferred orientation and 30 wadsleyite grains with a mean grain radius of 0.7 µm and

314   orientations concentrated between the (010) and (001) poles of the inverse pole figure. After full

315   conversion to wadsleyite (collection s08), we index 144 wadsleyite grains with a mean grain radius of

316   0.7 µm. The crystal preferred orientation is weak but shows two maxima at (001) and (010) in the

317   inverse pole figure.

318   **Grain size evolution**

319   Two tendencies are observed regarding grain size evolution in our experiments: i) in experiments

320   Olivine_01 and P2_01, the mean sample grain size decreases during the phase transition from olivine to

321   wadsleyite, while ii) in experiments LTC_03_02 and LTC_05_01, the grain size does not significantly

322   change during the phase transition.

323   The grains size evolution in experiments Olivine_01 and P2_01 is illustrated in Fig. 6, based on the

324   example of experiment P2_01 for which data with coexisting both olivine and wadsleyite is available.

325   Before the transformation (dataset s06), the olivine grain radii vary between 0.5 and 2.2 µm. During the

326   transformation, the olivine grain size decreases, with grain radii between 0.4 and 1.6 µm (dataset s07).

327   Coexisting wadsleyite in the same measurement shows grain radii between 0.4 and 1.1 µm. After the

328   transformation (dataset s08), the sample is made of wadsleyite grains with grain radii ranging between

329   0.2 and 1.8 μm and an average radius of 0.7 μm.

330   Regarding experiments LTC_03_02 and LTC_05_01, for which grain size does not reduce upon the

331   phase transformation to wadsleyite, we can notice that the average grain radius in olivine before

332   transformation is 0.5 μm. In all experiments, the mean radius of wadsleyite grains after full

333   transformation is above 0.5 μm. We can hence conclude that, in experiments LTC_03_02 and

334   LTC_05_01, olivine grain size before transformation is already close to that of the newly-formed

335   wadsleyite grains. The phase transformation hence does not result in grain size reduction in these

336   experiments.

337   Overall, the grain sizes in our experiments are small with an estimated mean grain size equal to or

338   smaller than 1 μm in equivalent radius (except for the starting single crystal of Olivine_01). The

339   differences in mean wadsleyite grain sizes between experiments can be explained by the grain size in

340   the starting material. Nevertheless, wadsleyite grain sizes are somewhat similar in all experiments and

341   we do not see a clear effect of the pressure medium. More investigations will be needed, however, to

342   conclude on the relative effects of stress, overpressure, and pressure media on wadsleyite grain sizes

343   after transformation. In all cases, large olivine crystals tend to disappear during the transformation,

344   with olivine grain radii of about 0.8 μm in equivalent radius in coexisting olivine and wadsleyite. The

345   wadsleyite grains past phase transformation have mean grain radii between 0.5 and 0.8 μm.

346 # DISCUSSION

347 **Olivine-wadsleyite transformation mechanism**

348   We observe lattice preferred orientations in wadsleyite after transformation, with [100]

349 crystallographic axis parallel or at 30–40° of the compression direction in experiments LTC_05_01 and

350 LTC_03_02 (Fig. 5). Starting from an olivine single-crystal (Olivine_01, Fig. 4), wadsleyite after

351 transformation also shows a similar LPO, although weaker than in experiments LTC_05_01 and

352 LTC_03_02.

353   Experiment P2_01, starting from polycrystalline olivine and for which measurements in the mixed

354 olivine-wadsleyite phase are available, shows a more complex behavior. The first wadsleyite grains

355 nucleate with orientations between the (010) and (001) poles of the IPF of the compression direction

356 (Fig. 5 s07). After the transformation (collection s08), the orientation distribution spreads, with clusters

357 of orientations near the (010), (001) and (100) poles of the IPF, which could be a transition between the

358 first nucleation texture (collection s07) and a texture with the [100] crystallographic axis parallel to

359 compression, as in the three other experiments.

360   A coherent transformation implies a crystallographic orientation relationship between the parent-

361 phase, olivine, and the daughter-phase, wadsleyite. Smyth et al. (2012) report two topotactic

362 relationships for the olivine–wadsleyite coherent transformation, based on observations in transmission

363 electron microscopy of post-mortem products of the transformation. Type I orientation relationships

364 lead to (100) olivine || {101} wadsleyite and [001] olivine || [010] wadsleyite. Type II orientation

365 relationships lead to {021} wadsleyite || (100) olivine and [100] wadsleyite || [001] olivine. Both Type I

366 and Type II orientation relationships are tested in Fig. 7 for experiments LTC_05_01 and LTC_03_02.

367 The results are clear: the orientations of wadsleyite grains observed in the experiment do not

368 correspond to the predictions of either Type I or Type II orientation relationships.

369 In P2_01, no clear LPO is observed in the olivine grains before the transformation or in the relict

370 olivine grains coexisting with wadsleyite during transformation. Based on our simulations (Fig. 7),

371 coherent transformations of polycrystalline olivine with no LPO should produce daughter-wadsleyite

372 with no LPO. However, the first wadsleyite grains observed during the transformation show a relatively

373 strong LPO along a girdle between the (010) and (001) poles of the IPF of the compression direction.

374 Hence a coherent transformation cannot explain the transformation texture (nor the post-transformation

375 texture) of the newly-formed wadsleyite in this experiment.

376   Experiments on polycrystalline olivine hence show that orientation relationships observed at the

377 local scale do not apply at the polycrystal scale. As discussed in Smyth et al. (2012), incoherent grains

378 of wadsleyite dominate the sample microstructure. This result is confirmed with experiment

379 Olivine_01, starting from a single crystal, in which multiple domains of wadsleyite and olivine are

380 formed during transformation, with no obvious orientation relation to the original single-crystal. As

381 such, the inheritance of crystallographic preferred orientations in the olivine-wadsleyite transformation

382 is unlikely to be significant at the 410 km depth discontinuity in the Earth mantle, with a dominant

383 incoherent nucleation of wadsleyite. LPO in wadsleyite during or after transformation is most likely

384 related to oriented growth due to stress or plastic deformation following the phase transformation.

385   Interestingly, the grain size observed in wadsleyite in our LH-DAC experiments is close to those

386 observed in multi-anvil press experiments at 1400-1800 K with durations ranging from tens of minutes

387 to a few hours (Nishihara et al., 2006, Demouchy et al., 2011, Mohiuddin and Karato, 2018). This

388 observation supports that transformation mechanisms in our LH-DAC experiments should not be

389 significantly different than that deduced from large-volume press experiments.

390 **Effect of grain size on the transformation mechanism**

391   The study of Kerschhofer et al. (1996) shows that the grain size of the transforming olivine

392 influences the olivine-wadsleyite transformation mechanism with i) a grain-boundary nucleation of

393 wadsleyite, operating in both a large single crystal and a fine grained matrix, and ii) an intracrystalline

394 nucleation of wadsleyite inside a large olivine single crystal only. None of these mechanisms are

395 reported to produce strict orientation relationships between olivine and wadsleyite.

396   In our polycrystalline experiments, the mean grain size of the parent-olivine is up to 1.0 μm in

397 equivalent radius, and hence is smaller than that of the fine matrix of the experiments of Kerschhofer

398 et al. (1996), where the grain-boundary nucleation is dominant. In experiment Olivine_01 the single-

399 crystal olivine sample is shown to subdivide into multiple domains of both olivine and wadsleyite as

400 the phase transition proceeds (e.g. Fig. 4), leading to an average grain radius of 0.8 μm both in olivine

401 and wadsleyite. According to Kerschhofer et al. (1996), the phase transition, in this case, should also be

402 controlled by a dominant grain-boundary nucleation mechanism.

403   Mohiuddin and Karato (2018) also found wadsleyite grains of small size (2.8-4.2 μm in diameter)

404 and proposed dominant grain-boundary nucleation of wadsleyite, but at the condition that the

405 transformation over-pressure is below 3 GPa. As over-pressure increases, they showed that intra-

406 crystalline nucleation makes a significant contribution to the volume fraction transformed. In our

407 experiments Olivine_01, LTC_05_01 and LTC_03_02, the transformation over-pressure is less or equal

408 to 3 GPa, and so should be dominated by grain-boundary nucleation of wadsleyite, in agreement with

409 the proposition of Kerschhofer et al. (1996). In experiment P2_01, although grain size is similar to that

410 of the other samples, the over-pressure is larger than 3 GPa. Thus, based on the results of Mohiuddin

411 and Karato (2018), a greater contribution of the intra-crystalline mechanism for wadsleyite nucleation

412 could be expected in this particular experiment.

413 **Effect of stress on the phase transformation**

414   Transformation mechanisms in the olivine system are known to be sensitive to parameters such as

415   stress, temperature, and over-pressure (e.g. Burnley and Green, 1989, Burnley, 1995, Kerschhofer et al,

416   1996, 1998, Smyth et al, 2012, and references therein). Early diamond anvil cell experiments provided

417   inconsistent results, probably due to the lack of pressure-transmitting media and high stresses (Burnley

418   1995).

419   Our experiments are performed at much higher temperatures, thanks to laser heating, and use

420   different pressure media, MgO, Alumina, and KCl, all with different strengths. They lead to consistent

421   results: the wadsleyite microstructures after transformation from olivine are dominated by an

422   incoherent mechanism, whatever the pressure medium or over-pressure prior to the transformation,

423   with no effect of the olivine starting texture or grain sizes, and consistent grain sizes in wadsleyite past

424   transformation (e.g. Table 2). This is consistent with observations in low-stress and small grain sizes

425   experiments in large-volume press experiments (e.g. Burnley and Green, 1989, Kerschhofer et al, 1996,

426   Smyth et al, 2012). A more precise analysis of the effect of stress on the phase transformation

427   mechanism would require a proper estimate of stress in the olivine and wadsleyite grains. Grain-to-

428   grain stress estimate can be obtained using 3D-XRD (e.g. Oddershede et al, 2010, Chandler et al, 2021)

429   but requires careful calibration for relevant measurements. We did attempt to extract grain-level stress

430   distributions from our datasets but did not obtain reliable results. This will have to be the topic of future

431   investigations.

432   Over-pressure, stress, and subsequent deformation may have affected details of grain orientations in

433   wadsleyite past transformation from olivine (e.g. Figs 4, 5), but the fine analysis of these features goes

434   beyond the goals of this paper.

IMPLICATIONS

435

436   Olivine and wadsleyite are considered the main minerals of the upper mantle and the upper section

437   of the MTZ, respectively. Hence, microstructures in these phases have a great influence on the

438   properties of these two layers. It is now largely accepted that LPO induced by olivine deformation is

439   the source of the strong seismic anisotropy measured in the upper mantle (Nishimura and Forsyth,

440   1989; Cara and Lévêque, 1988; Long and Becker, 2010). Textured downwelling olivine of the upper

441   mantle then transforms into wadsleyite at depths of the 410 km depth discontinuity and questions arise

442   whether this LPO will propagate to wadsleyite in the MTZ.

443   In agreement with previous ex-situ studies based on electron microscopy (Brearley et al., 1992;

444   Kerschhofer et al., 1996, 1998; Kubo et al., 1998b, 2004; Smyth et al., 2012; Mohiuddin and Karato,

445   2018), our in-situ high pressure high temperature measurements show that the transformation is

446   dominated by incoherent nucleation at pressures between 12.3 and 20.2 GPa, and temperatures of

447   1450–1770 K. The result is also confirmed by experiments starting from a larger single-crystal olivine

448   grain.

449   Thus, our results argue that the olivine to wadsleyite transformation around the 410 km depth will

450   erase the LPO and, also, the whole microstructure of the parent-olivine. As such, the olivine to

451   wadsleyite phase transformation cannot be a source of LPO in the transition zone. Accordingly, seismic

452   anisotropy in olivine will be erased as rocks cross the 410 km depth discontinuity. This is consistent

453   with seismic observations from the literature, that report a significant decrease of the seismic

454   anisotropy in the MTZ compared to the upper mantle (e.g. Fischer and Wien, 1996; Panning and

455   Romanowicz, 2006; Foley and Long, 2011; Yuan and Beghein, 2013; Huang et al., 2019). Based on

456   these results, the seismic anisotropy observed in this region (Panning and Romanowicz, 2006; Yuan

457 and Beghein, 2013; Foley and Long, 2011; Huang et al., 2019) should rather arise from additional

458 plastic deformation below the transition zone.

459   After transformation, the size of the resulting wadsleyite grains in our experiments ranges between

460 0.4 and 0.8 μm in mean equivalent radius. This result is consistent with other experimental studies on

461 the olivine-wadsleyite transformation, where the newly formed wadsleyite grains are generally on the

462 order of micrometers or tens of micrometers (Smyth et al., 2012; Perrillat et al., 2013; Rosa et al., 2016;

463 Mohiuddin and Karato, 2018). Hence, if the grain size of the parent olivine is larger, as it may be

464 expected in the upper mantle (mm to cm, Faul and Jackson, 2005), the transformation would imply a

465 grain size reduction. Grain size is an important parameter in the mechanical properties of rocks as it can

466 change the dominant deformation mechanism of the aggregate. This change of dominant deformation

467 mechanisms (dislocation creep vs. diffusion creep vs. grain boundary sliding) due to grain size

468 variations in the mantle was investigated by numerical studies (e.g. Rozel, 2012; Dannberg et al.,

469 2017), which show that grain size variations can modify the rheology and convection of the mantle. In

470 addition, using numerical calculations based on experimental data, Mohiuddin and Karato (2018) show

471 that slab materials at lower temperatures (i.e. small grain size) will be weaker than slabs at higher

472 temperatures (large grain size) due to sluggish grain growth. According to our measurements, the

473 olivine-wadsleyite phase transformation will nucleate small wadsleyite grains, and hence induce a

474 weakening of the aggregate, which will be important to model deformation and the dynamics of the

475 Earth's transition zone.

476   Finally, the study highlights the potential of using multigrain X-ray diffraction in the laser-heated

477 diamond anvil cell for the study of microstructures in Earth mantle minerals. Unlike other techniques,

478 such as radial x-ray diffraction, multigrain X-ray diffraction can be combined with laser-heating,

479 approaching both relevant mantle pressure and temperature conditions, and maintaining a low level of

480   stress on the sample. In addition, the method allows for extracting statistical information on individual

481   grain sizes and orientations, hence offering new avenues for discoveries in high pressure mineralogical

482   science.

483   <div align="center">**FUNDING**</div>

489   <div align="center">**ACKNOWLEDGMENTS**</div>

503

REFERENCES

505   Akaogi, M., Ito, E., and Navrotsky, A. (1989) Olivine-modified spinel-spinel transitions in the
506   system Mg_2SiO_4-Fe_2SiO_4: Calorimetric measurements, thermochemical calculation, and geophysical
507   application, Journal of Geophysical Research: Solid Earth, 94, 15,671–15,685,
508   10.1029/JB094iB11p15671.

509   Angel, R.J., Alvaro, M., and Gonzalez-Platas, J. (2014) Eosfit7c and a fortran module (library) for
510   equation of state calculations, Zeitschrift für Kristallographie - Crystalline Materials, 229,
511   10.1515/zkri-2013-1711.

512   Angel, R.J., Alvaro, M., and Nestola, F. (2018) 40 years of mineral elasticity: a critical review and a
513   new parameterisation of equations of state for mantle olivines and diamond inclusions, Physics and
514   Chemistry of Minerals, 45, 95–113, 10.1007/s00269-017-0900-7.

515   Bachmann, F., Hielscher, R., and Schaeben, H. (2010) Texture analysis with MTEX - free and open
516   source software toolbox, Solid State Phenomena, 160, 63–68, 10.4028/www.scientific.net/SSP.160.63.

517   Bercovici, D., and Karato, S. (2003) Whole-mantle convection and the transition-zone water filter,
518   Nature, 425, 39–44, 10.1038/nature01918.

519   Brearley, A.J., Rubie, D.C., and Ito, E. (1992) Mechanisms of the transformations between the α, β
520   and γ polymorphs of Mg_2SiO_4 at 15 GPa, Physics and Chemistry of Minerals, 18, 343–358.

521   Burnley, P.C., and Green, H.W. (1989) Stress dependence of the mechanism of the olivine–spinel
522   transformation, Nature, 338, 753–756, 10.1038/338753a0.

523   Burnley, P.C., Bassett, W.A, and Wu T.C (1995), Diamond anvil cell study of the transformation
524   mechanism from the olivine to spinel phase in Co_2SiO_4, Ni_2SiO_4, and Mg_2GeO_4, Journal of
525   Geophysical Research: Solid Earth, 100(B9), 17715-17723, doi: 10.1029/95JB01578.

526   Bykova, E., Aprilis, G., Bykov, M., Glazyrin, K., Wendt, M., Wenz, S., Liermann, H.P., Roeh, J.T.,
527   Ehnes, A., Dubrovinskaia, N., et al. (2019) Single-crystal diffractometer coupled with double-sided
528   laser heating system at the extreme conditions beamline P02.2 at PETRA III, Review of Scientific
529   Instruments, 90, 073,907.

530   Cara, M., and Lévêque, J.J. (1988) Anisotropy of the asthenosphere: The higher mode data of the
531 pacific revisited, Geophysical Research Letters, 15, 205–208, 10.1029/GL015i003p00205.

532   Chandler, B., Bernier, J., Diamond, M., Kunz, M., and Wenk, H.R. (2021a) Exploring
533 microstructures in lower mantle mineral assemblages with synchrotron x-rays, Science Advances, 7,
534 eabd3614, 10.1126/sciadv.abd3614.

535   Chandler, B., Devoe, M., Kunz, M., and Wenk, H.R. (2021b) Using multigrain crystallography to
536 explore the microstructural evolution of the α-olivine to γ-ringwoodite transformation and ε-Mg_2SiO_4
537 at high pressure and temperature, Minerals, 11, 424, 10.3390/min11040424.

538   Dannberg, J., Eilon, Z., Faul, U., Gassmöller, R., Moulik, P., and Myhill, R. (2017) The importance
539 of grain size to mantle dynamics and seismological observations, Geochemistry, Geophysics,
540 Geosystems, 18, 3034–3061, 10.1002/2017GC006944.

541   Demouchy, S., Mainprice, D., Tommasi, A., Couvy, H., Barou, F., Frost, D. J., and Cordier, P.
542 (2011). Forsterite to wadsleyite phase transformation under shear stress and consequences for the
543 Earth's mantle transition zone, Physics of the Earth and Planetary Interiors, 184(1-2), 91-104,
544 10.1016/j.pepi.2010.11.001.

545   Dziewoński, A.M., and Anderson, D.L. (1981) Preliminary reference Earth model, Physics of the
546 Earth and Planetary Interior, 25, 297–356, 10.1016/0031-9201(81)90046-7.

547   Eikenberry, E., Brönnimann, C., Hülsen, G., Toyokawa, H., Horisberger, R., Schmitt, B., Schulze-
548 Briese, C., and Tomizaki, T. (2003) PILATUS: a two-dimensional x-ray detector for macromolecular
549 crystallography, Nuclear Instruments and Methods in Physics Research Section A: Accelerators,
550 Spectrometers, Detectors and Associated Equipment, 501, 260–266, 10.1016/S0168-9002(02)02044-2.

551   Faul, U., and Jackson, I. (2005) The seismological signature of temperature and grain size
552 variations in the upper mantle, Earth and Planetary Science Letters, 234, 119–134,
553 10.1016/j.epsl.2005.02.008.

554   Fischer, K.M., and Wien, D.A. (1996) The depth distribution of mantle anisotropy beneath the
555 tonga subduction zone, Earth and Panetary Science Letters, pp. 253–260.

556   Foley, B.J., and Long, M.D. (2011) Upper and mid-mantle anisotropy beneath the Tonga slab:
557 Anisotropy beneath Tonga slab, Geophysical Research Letters, 38, L02,303, 10.1029/2010GL046021.

558   Helffrich, G.R., and Wood, B.J. (1996) 410 km discontinuity sharpness and the form of the olivine
559 α–β phase diagram: resolution of apparent seismic contradictions, Geophysical Journal International,
560 126, F7–F12, 10.1111/j.1365-246X.1996.tb05292.x.

561   Huang, Q., Schmerr, N., Waszek, L., and Beghein, C. (2019) Constraints on seismic anisotropy in
562 the mantle transition zone from long-period SS precursors, Journal of Geophysical Research: Solid
563 Earth, 124, 6779–6800, 10.1029/2019JB017307.

564   Ito, E., and Katsura, T. (1989) A temperature profile of the mantle transition zone, Geophysical
565 Research Letters, 16, 425–428, 10.1029/GL016i005p00425.

566   Katsura, T., and Ito, E. (1989) The system Mg_2SiO_4-Fe_2SiO_4 at high pressures and temperatures:
567   Precise determination of stabilities of olivine, modified spinel, and spinel, Journal of Geophysical
568   Research: Solid Earth, 94, 15,663–15,670, 10.1029/JB094iB11p15663.

569   Katsura, T., Yamada, H., Nishikawa, O., Song, M., Kubo, A., Shinmei, T., Yokoshi, S., Aizawa, Y.,
570   Yoshino, T., Walter, M.J., Ito, E., and Funakoshi, K.i. (2004) Olivine-wadsleyite transition in the
571   system $(Mg,Fe)_2SiO_4$, Journal of Geophysical Research: Solid Earth, 109, B02,209,
572   10.1029/2003JB002438.

573   Katsura, T., Shatskiy, A., Manthilake, M.A.G.M., Zhai, S., Yamazaki, D., Matsuzaki, T., Yoshino,
574   T., Yoneda, A., Ito, E., Sugita, M., Tomioka, N., Nozawa, A., and Funakoshi, K.i. (2009) P-V-T
575   relations of wadsleyite determined by in situ X-ray diffraction in a large-volume high-pressure
576   apparatus, Geophysical Research Letters, 36, L11,307, 10.1029/2009GL038107.

577   Kavner, A., and Duffy, T. S. (2001), Pressure–volume–temperature paths in the laser-heated
578   diamond anvil cell, Journal of Applied Physics, 89(3), 1907-1914, 10.1063/1.1335827.

579   Kerschhofer, L., Sharp, T.G., and Rubie, D.C. (1996) Intracrystalline transformation of olivine to
580   wadsleyite and ringwoodite under subduction zone, Science, 274, 79.

581   Kerschhofer, L., Dupas, C., Liu, M., Sharp, T.G., Durham, W.B., and Rubie, D.C. (1998)
582   Polymorphic transformations between olivine, wadsleyite and ringwoodite: mechanisms of
583   intracrystalline nucleation and the role of elastic strain, Mineralogical Magazine, 62, 617–638,
584   10.1180/002646198548016.

585   Kimura, T., Ohfuji, H., Nishi, M., and Irifune, T. (2017) Melting temperatures of MgO under high
586   pressure by micro-texture analysis, Nature Communication, 8, 10.1038/ncomms15735.

587   Kubo, T., Ohtani, E., Kato, T., Shinmei, T., and Fujino, K. (1998a) Effects of water on the alpha-
588   beta transformation kinetics in san carlos olivine, Science, 281, 85–87.

589   Kubo, T., Ohtani, E., Kato, T., Shinmei, T., and Fujino, K. (1998b) Experimental investigation of
590   the α–β transformation of San Carlos olivine single crystal, Physics and Chemistry of Minerals, 26, 1–
591   6.

592   Kubo, T., Ohtani, E., and Funakoshi, K.I. (2004) Nucleation and growth kinetics of the α–β
593   transformation in Mg_2SiO_4 determined by in-situ synchrotron powder X-ray diffraction, American
594   Mineralogist, 89, 285–293.

595   Langrand, C., Hilairet, N., Nisr, C., Roskosz, M., Ribárik, G., Vaughan, G.B.M., and Merkel, S.
596   (2017) Reliability of multigrain indexing for orthorhombic polycrystals above 1 Mbar: application to
597    $MgSiO_3$ post-perovskite, Journal of Applied Crystallography, 50, 120–130,
598   10.1107/S1600576716018057.

599   Ledoux, E., Krug, M., Gay, J., Chantel, J., Hilairet, N., Bykov, M., Bykova, E., Aprilis, G.,

600   Svitlyk, V., Garbarino, G., Guignot, N., Sanchez-Valle, C., Speziale, S., Merkel, S. (2023), Data
601   supporting the article "In-situ study of microstructures induced by the olivine to wadsleyite
602   transformation at conditions of the 410 km depth discontinuity" by Ledoux et al.",
603   https://doi.org/10.57745/NZFWP9, Recherche Data Gouv. Temporary link prior to publication:

604   https://entrepot.recherche.data.gouv.fr/privateurl.xhtml?token=fa50ff28-cc1b-4374-8013-
605   88950af2c276.

606   Liermann, H.P., Konôpková, Z., Morgenroth, W., Glazyrin, K., Bednarik, J., McBride, E.E.,
607   Petitgirard, S., Delitz, J.T., Wendt, M., Bican, Y., Ehnes, A., Schwark, I., Rothkirch, A., Tischer, M.,
608   Heuer, J., Schulte-Schrepping, H., Kracht, T., and Franz, H. (2015) The extreme conditions beamline
609   P02.2 and the extreme conditions science infrastructure at PETRA III, Journal of Synchrotron
610   Radiation, 22, 908–924, 10.1107/S1600577515005937.

611   Long, M.D., and Becker, T.W. (2010) Mantle dynamics and seismic anisotropy, Earth and Planetary
612   Science Letters, 297, 341–354.

613   Lutterotti, L., Vasin, R., and Wenk, H.R. (2014) Rietveld texture analysis from synchrotron
614   diffraction images. I. calibration and basic analysis, Powder Diffraction, 29, 76–84,
615   10.1017/S0885715613001346.

616   Mohiuddin, A., and Karato, S.I. (2018) An experimental study of grain-scale microstructure
617   evolution during the olivine-wadsleyite phase transition under nominally 'dry' conditions, Earth and
618   Planetary Science Letters, 501, 128–137, 10.1016/j.epsl.2018.08.039.

619   Mohiuddin, A., Karato, S.I., and Girard, J. (2020) Slab weakening during the olivine to ringwoodite
620   transition in the mantle, Nature Geoscience, 13, 170–174, 10.1038/s41561-019-0523-3.

621   Nishihara, Y., Shinmei, T., and Karato, S. I. (2006), Grain-growth kinetics in wadsleyite: effects of
622   chemical environment, Physics of the Earth and Planetary Interiors, 154(1), 30-43,
623   10.1016/j.pepi.2005.08.002.

624   Nishimura, C.E., and Forsyth, D.W. (1989) The anisotropic structure of the upper mantle in the
625   pacific, Geophysical Journal International, 96, 203–229, 10.1111/j.1365-246X.1989.tb04446.x.

626   Nisr, C., Ribárik, G., Ungár, T., Vaughan, G.B.M., Cordier, P., and Merkel, S. (2012) High
627   resolution three-dimensional x-ray diffraction study of dislocations in grains of $MgGeO_3$ post-
628   perovskite at 90 GPa, Journal of Geophysical Research: Solid Earth, 117, 10.1029/2011JB008401.X

629   Nisr, C., Ribárik, G., Ungár, T., Vaughan, G.B., and Merkel, S. (2014) Three-dimensional x-ray
630   diffraction in the diamond anvil cell: application to stishovite, High Pressure Research, 34, 158–166,
631   10.1080/08957959.2014.885021.

632   Oddershede, J., Schmidt, S., Poulsen, H. F., Sørensen, H. O., Wright, J., and Reimers, W., (2010)
633   Determining grain resolved stresses in polycrystalline materials using three-dimensional X-ray
634   diffraction, Journal of Applied Crystallography, 43, 539-549, doi: 10.1107/S0021889810012963.

635   Panning, M., and Romanowicz, B. (2006) A three-dimensional radially anisotropic model of shear
636   velocity in the whole mantle, Geophysical Journal International, 167, 361–379, 10.1111/j.1365-
637   246X.2006.03100.x.

638   Perrillat, J.P., Daniel, I., Bolfan-Casanova, N., Chollet, M., Morard, G., and Mezouar, M. (2013)
639   Mechanism and kinetics of the α–β transition in San Carlos olivine $Mg_{1.8}Fe_{0.2}SiO_4$: Kinetics of α–β
640   transition in olivine, Journal of Geophysical Research: Solid Earth, 118, 110–119,
641   10.1002/jgrb.50061.X

642   Prescher, C., and Prakapenka, V.B. (2015) DIOPTAS: a program for reduction of two-dimensional
643   x-ray diffraction data and data exploration, High Pressure Research, 35, 223–230,
644   10.1080/08957959.2015.1059835.

645   Poirier, J. P., & Guillopé, M. (1979). Deformation induced recrystallization of minerals. Bulletin de
646   Mineralogie, 102(2), 67-74.

647   Ringwood, A. (1991) Phase transformations and their bearing on the constitution and dynamics of
648   the mantle, Geochimica Cosmochima Acta, 55, 2083–2110, 10.1016/0016-7037(91)90090-r.

649   Ringwood, A.E. (1958) The constitution of the mantle - II further data on the olivine-spinel
650   transition, Geochimica et Cosmochimica Acta, 15, 18-20.

651   Ringwood, A.E. (1962) Prediction and confirmation of olivine-spinel transition in Ni_2SiO_4,
652   Geochimica et Cosmochimica Acta, 26, 457–469, 10.1016/0016-7037(62)90090-X.

653   Ringwood, A.E., and Seabrook, M. (1962) Olivine-spinel equilibria at high pressure in the system
654   Ni_2GeO_4-Mg_2SiO_4, Journal of Geophysical Research, 67, 1975–1985, 10.1029/JZ067i005p01975.

655   Rosa, A.D., Hilairet, N., Ghosh, S., Garbarino, G., Jacobs, J., Perrillat, J.P., Vaughan, G., and
656   Merkel, S. (2015) In situ monitoring of phase transformation microstructures at Earth's mantle pressure
657   and temperature using multi-grain XRD, Journal of Applied Crystallography, 48, 1346–1354,
658   10.1107/S1600576715012765.

659   Rosa, A.D., Hilairet, N., Ghosh, S., Perrillat, J.P., Garbarino, G., and Merkel, S. (2016) Evolution of
660   grain sizes and orientations during phase transitions in hydrous Mg_2SiO_4, Journal of Geophysical
661   Research: Solid Earth, 121, 1-16, 10.1002/2016JB013360

662   Ross, N.L., and Navrotsky, A. (1987) The Mg_2GeO_4 olivine-spinel phase transition, Physics and
663   Chemistry of Minerals, 14, 473–481, 10.1007/BF00628825.X

664   Rozel, A. (2012) Impact of grain size on the convection of terrestrial planets: Convection and grain
665   size, Geochemistry, Geophysics, Geosystems, 13, Q10,020, 10.1029/2012GC004282.

666   Saki, M., Thomas, C., Merkel, S., and Wookey, J. (2018) Detecting seismic anisotropy above the
667   410 km discontinuity using reflection coefficients of underside reflections, Physics of the Earth and
668   Planetary Interiors, 274, 170–183, 10.1016/j.pepi.2017.12.001.

669   Schmidt, S. (2014) GrainSpotter: a fast and robust polycrystalline indexing algorithm, Journal of
670   Applied Crystallography, 47, 276–284, 10.1107/S1600576713030185.

671   Shen, G., and Lazor, P. (1995) Measurement of melting temperatures of some minerals under lower
672   mantle pressures, Journal of Geophysical Research: Solid Earth, 100, 17,699–17,713,
673   10.1029/95jb01864.

674   Smyth, J.R., Miyajima, N., Huss, G.R., Hellebrand, E., Rubie, D.C., and Frost, D.J. (2012) Olivine-
675   wadsleyite-pyroxene topotaxy: Evidence for coherent nucleation and diffusion-controlled growth at the
676   410-km discontinuity, Physics of the Earth and Planetary Interiors, 200-201, 85–91,
677   10.1016/j.pepi.2012.04.003.

678   Sörensen, H.O., Schmidt, S., Wright, J.P., Vaughan, G.B.M., Techert, S., Garman, E.F., Oddershede,
679 J., Davaasambu, J., Paithankar, K.S., Gundlach, C., and Poulsen, H.F. (2012) Multigrain
680 crystallography, Zeitschrift für Kristallographie - Crystalline Materials, 227, 63-78.

681   Urai, J. L., Means, W. D., and Lister, G. S. (1986), Dynamic recrystallization of minerals, Mineral
682 and rock deformation: laboratory studies, 36, 161-199, 10.1029/GM036p0161.

683   Vaughan, P.J., and Coe, R.S. (1981) Creep mechanism in Mg_2GeO_4: Effects of a phase transition,
684 Journal of Geophysical Research, 86, 389, 10.1029/JB086iB01p00389.

685   Wenk, H.R., Lonardelli, I., Pehl, J., Devine, J., Prakapenka, V., Shen, G., and Mao, H.K. (2004) In
686 situ observation of texture development in olivine, ringwoodite, magnesiowüstite and silicate
687 perovskite at high pressure, Earth and Planetary Science Letters, 226, 507–519,
688 10.1016/j.epsl.2004.07.033.

689   Wenk, H.R., Lutterotti, L., Kaercher, P., Kanitpanyacharoen, W., Miyagi, L., and Vasin, R. (2014)
690 Rietveld texture analysis from synchrotron diffraction images. II. Complex multiphase materials and
691 diamond anvil cell experiments, Powder Diffraction, 29, 220–232, 10.1017/S0885715614000360.

692   Wright, J.P. (2006) ImageD11, ESRF, Grenoble, France, https://github.com/FABLE-
693 3DXRD/ImageD11.

694   Yuan, K., and Beghein, C. (2013) Seismic anisotropy changes across upper mantle phase
695 transitions, Earth and Planetary Science Letters, 374, 132–144, 10.1016/j.epsl.2013.05.031.

696   Zhang, L., Yuan, H., Meng, Y., and Mao, H.K. (2019) Development of high-pressure multigrain x-
697 ray diffraction for exploring the earth's interior, Engineering, 5, 441–447, 10.1016/j.eng.2019.02.004.

698   Zhou, D., Dong, J., Si, Y., Zhu, F., and Li, J. (2020) Melting curve of potassium chloride from in
699 situ ionic conduction measurements, Minerals, 10, 250, 10.3390/min10030250.

700

701   TABLES

702

Experiment	Starting material	PTM	Beamline	Characterization technique
Olivine_01	Single crystal	Alumina	SOLEIL-PSICHÉ	MGC after temperature quench
LTC_05_01	Polycrystal	MgO	ESRF-ID27	In-situ MGC at high temperature
LTC_03_02	Polycrystal	MgO	ESRF-ID27	In-situ MGC at high temperature
P2_01	Polycrystal	KCl	PETRA-III-P02.2	In-situ MGC at high temperature

703

704   Table 1: List of samples and experiments. PTM stands for Pressure Transmitting Medium.

705

706

Experiment	Collection	P (GPa)	T (K)	Phase	N	Mean GR (µm)	GVE per grain	Indexed GVE
Olivine_01	multi1	6.3	300	olivine	1	6.1	75.0	19.9%
	multi4	16.1	300	olivine	25	0.8(3)	31.0	16.4%
				wadsleyite	72	0.8(3)	31.7	42.6%
LTC_05_01	s26	14.9	1400	olivine	55	0.5(3)	37.9	23.3%
	s27	18.7	1730	wadsleyite	114	0.6(3)	39.0	46.4%
LTC_03_02	s07	17.0	1700	olivine	180	0.5(3)	46.9	58.7%
	s08	18.8	1700	wadsleyite	188	0.5(3)	49.4	63.2%
P2_01	s06	20.2	1550	olivine	84	1.0(4)	122.4	47.6%
	s07	13.5	1510	olivine	83	0.7(3)	119.1	46.8%
				wadsleyite	30	0.7(2)	123.7	17.0%
	s08	12.3	1450	wadsleyite	144	0.7(3)	47.4	76.2%

707

708   Table 2: Experimental conditions and indexing statistics. For each experiment, the table indicates

709   the pressure (P)/temperature (T) conditions at which multigrain measurements were performed,

710   together with the results of the multigrain crystallography indexing: number of indexed olivine or

711   wadsleyite grains (N), the mean radius of the indexed grains (mean GR), the mean number of indexed

712   reflections per grain (Gve per grains), and percentage of indexed G vectors for each phase (Indexed

713   Gve). Note that other phases, such as the pressure medium, might also be the source of a large number

714   of G vectors that overlap with those of the phase of interest and will reduce the apparent percentage of

715   indexed G vectors. Also note that the mean grain radius deduced from MGC in experiment Olivine_01

716   is limited by the size of the incoming X-ray beam, and hence smaller than that of the original single-

717   crystal. Numbers in parenthesis are standard deviations from the mean grain size, on the last digit.

718   **FIGURES**
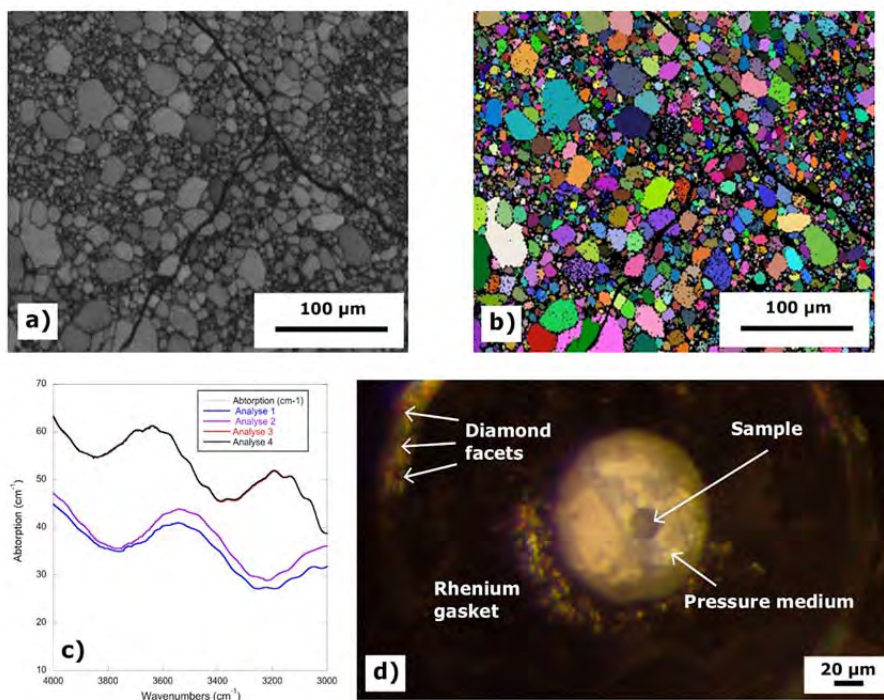

719

720   Figure 1: Characterization of the polycrystalline starting material for experiments at ESRF and

721   PETRA III. a) EBSD band contrast image showing the shapes and sizes of the grains in the olivine

722   polycrystal after piston-cylinder sintering; b) EBSD orientation map of the starting material; c) FTIR

723   measurements of water content in grains of the sintered polycrystal; d) Photograph of the diamond

724   anvil cell pressure chamber (closed cell, top view). The olivine polycrystalline sample is a 20 μm

725   diameter disk loaded with a MgO pressure medium inside a 140 μm diameter hole in a rhenium gasket.

726
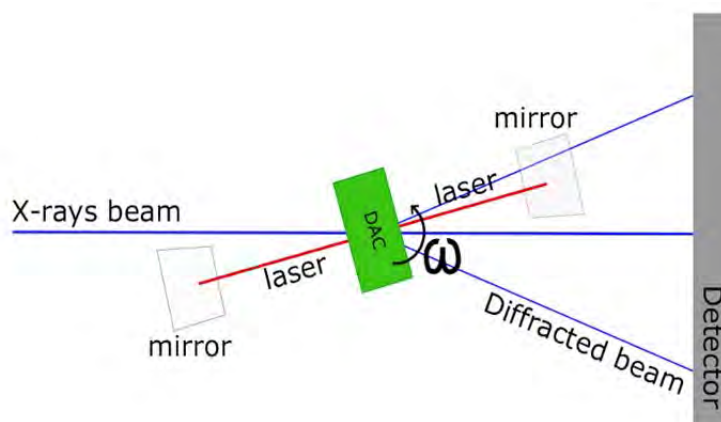
Figure 2: Experimental layout for multigrain crystallography (MGC) measurements at high

pressure and high temperature at a synchrotron beamline. View from the top. The synchrotron X-rays

beam (thick blue line) passes through the DAC (in green) and is transmitted or diffracted by the

crystallites in the sample. The diffracted rays (thin blue lines) form the diffraction pattern on the

detector (in grey). The DAC is rotated in ω and data is collected at different ω values. In the reported

experiments at both PETRA-III-P02.2 and ESRF-ID27, the laser heating system was rotating with the

DAC during ω rotations. At SOLEIL-PSICHÉ, the lasers were fixed and the sample was quenched in

temperature before collecting MGC data.
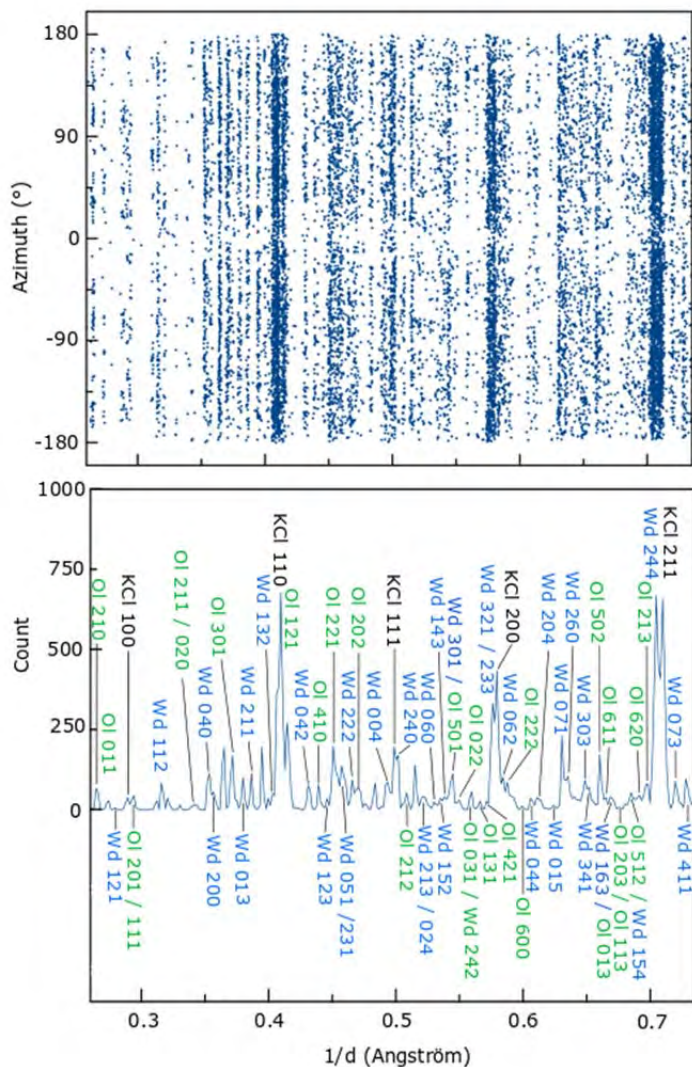
735

736

737   Figure 3: Experimental diffraction data for dataset P2_01_s07 where both olivine and wadsleyite

738   coexist. (a) Diffraction spots extracted by the 3D-XRD process from the whole diffraction collection,

739   plotted in azimuth vs. inverse d-spacing and staked in omega. (b) Integrated diffraction pattern with

740   annotated diffraction peaks for KCl, olivine and wadsleyite. Here, the diffraction pattern is plotted as a

741   histogram of locations of the diffraction spots shown in (a) vs. inverse of the d-spacing. Using such a

742   histogram leads to sharp diffraction signals and allows for easy sample identification.

743
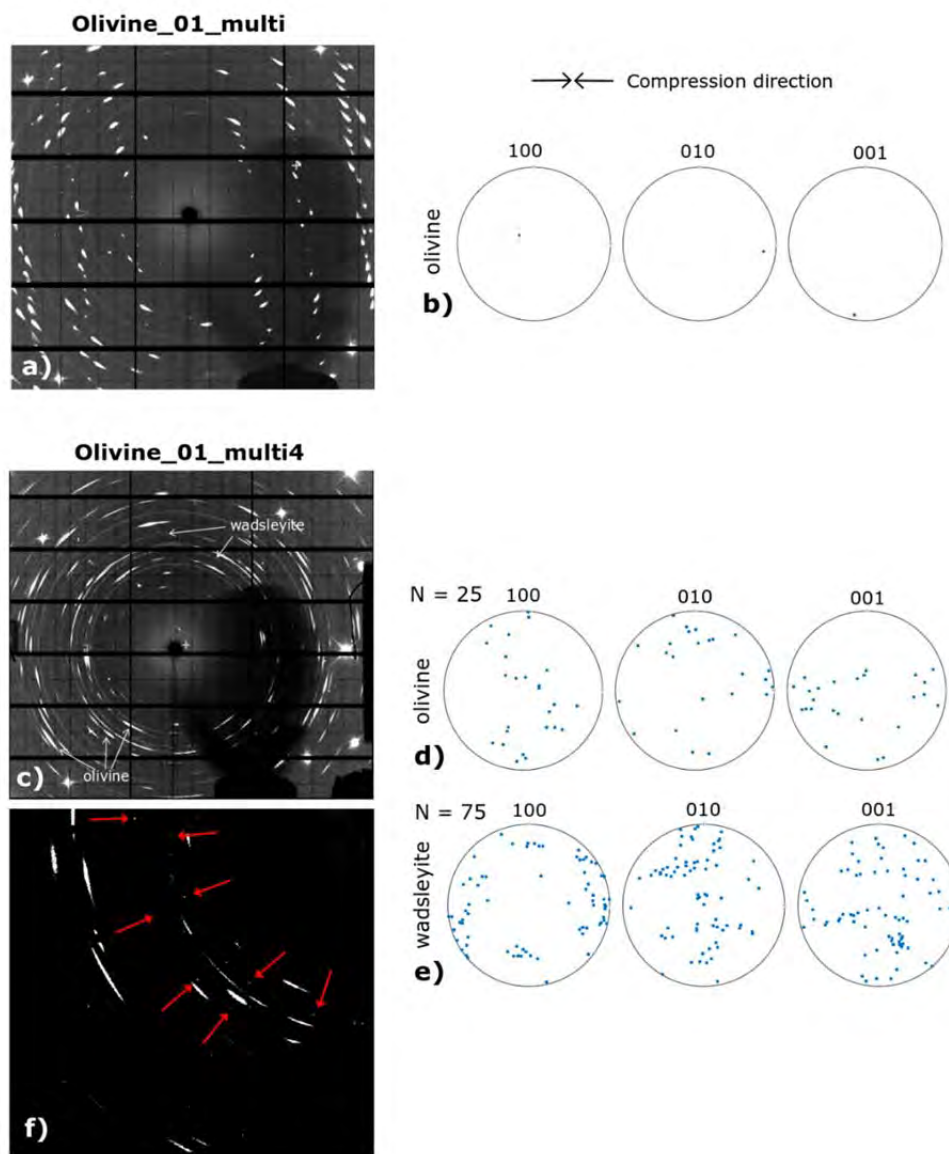
744

745 Figure 4: Transformation microstructures starting from an olivine single crystal. Single crystal

746 olivine data (a,b), olivine-wadsleyite polycrystal data after partial transformation (c, d, e). Stacked

747 diffraction patterns (a,c). (100), (010) and (001) pole figures representing the orientations of olivine

748 (b,d) and wadsleyite grains (e). The compression direction is indicated above the pole figures. To better

749 illustrate the diffraction spots of the wadsleyite grains, a zoom-in for one image at one omega step of

750 the collection is shown (f).
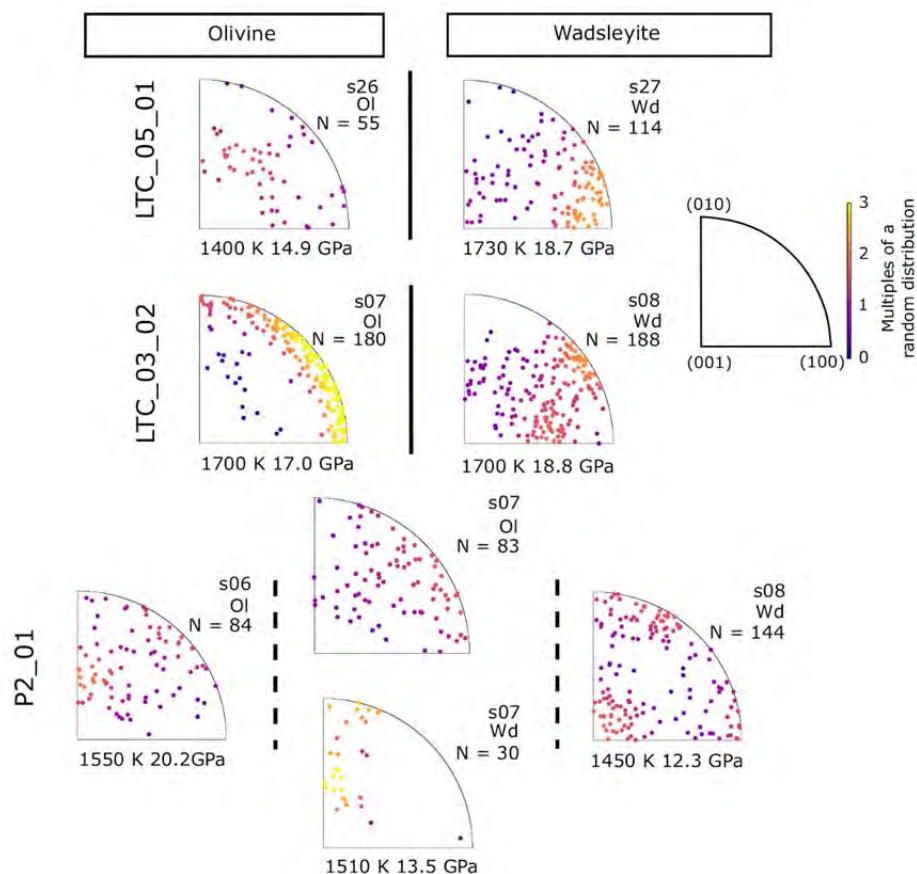
751

752   Figure 5: Transformation microstructures in polycrystalline olivine samples. Inverse pole figures of

753   the compression direction representing grain orientations of olivine (Ol) before transformation, olivine

754   (Ol) and wadsleyite (Wd) during transformation, and wadsleyite (Wd) after transformation from

755   olivine. LTC_05_01, LTC_03_02 and P2_01 are different experiments. Pressure and temperature

756   conditions of the measurements are indicated below each inverse pole figure along with N, the number

757   of indexed grains. The fundamental space and axes defining the inverse pole figure are shown on the

758   right. The color scale applied to the markers is based on a probability calculated from the orientation

759   distribution function fitted to the sample and is expressed in multiple of a random distribution (m.r.d).

760   It should be noted that, in all the experiments in this figure, MGC data collections were performed in

761   situ at high P-T conditions during laser-heating.

762
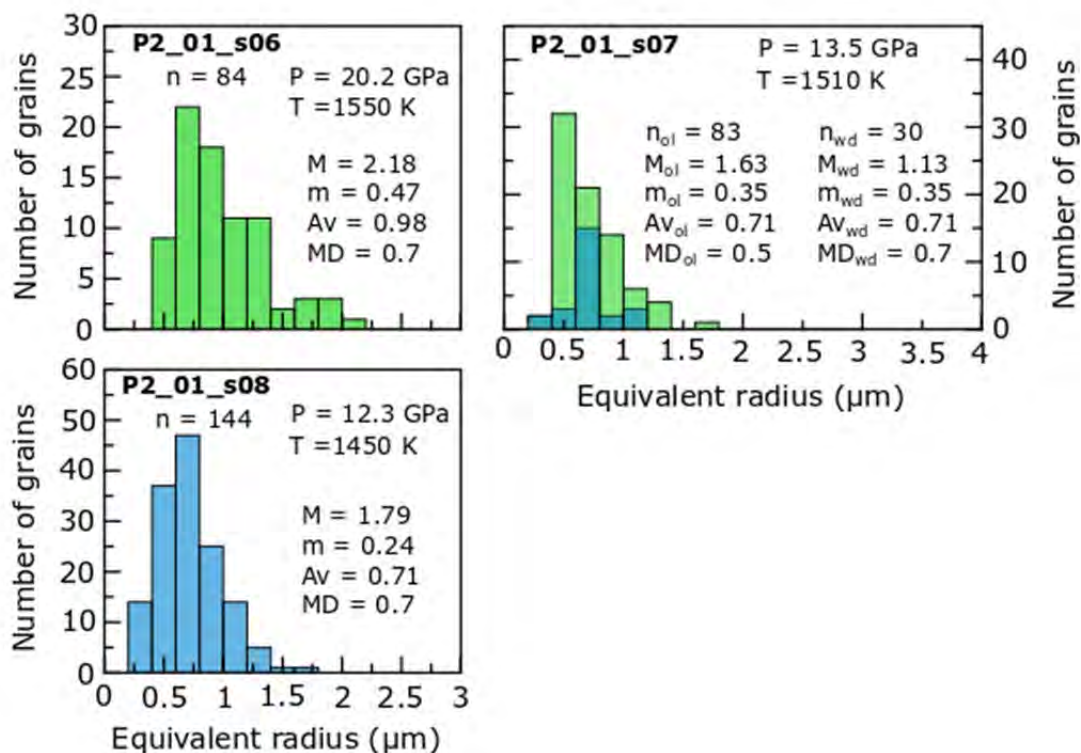
763

764   Figure 6: Distribution of estimated grain equivalent radii in experiment P2_01 while the sample is

765   pure olivine (collection s06), a mixed olivine-wadsleyite phase (collection s07) and fully transformed

766   to wadsleyite (collection s08). The green and blue bars correspond to olivine and wadsleyite grains

767   size, respectively. n is the number of grains for each phase. M, m, Av are the maximum, minimum, and

768   average grain radii, respectively. MD is the grain radius for which distribution is maximal. All are

769   expressed in μm.

770
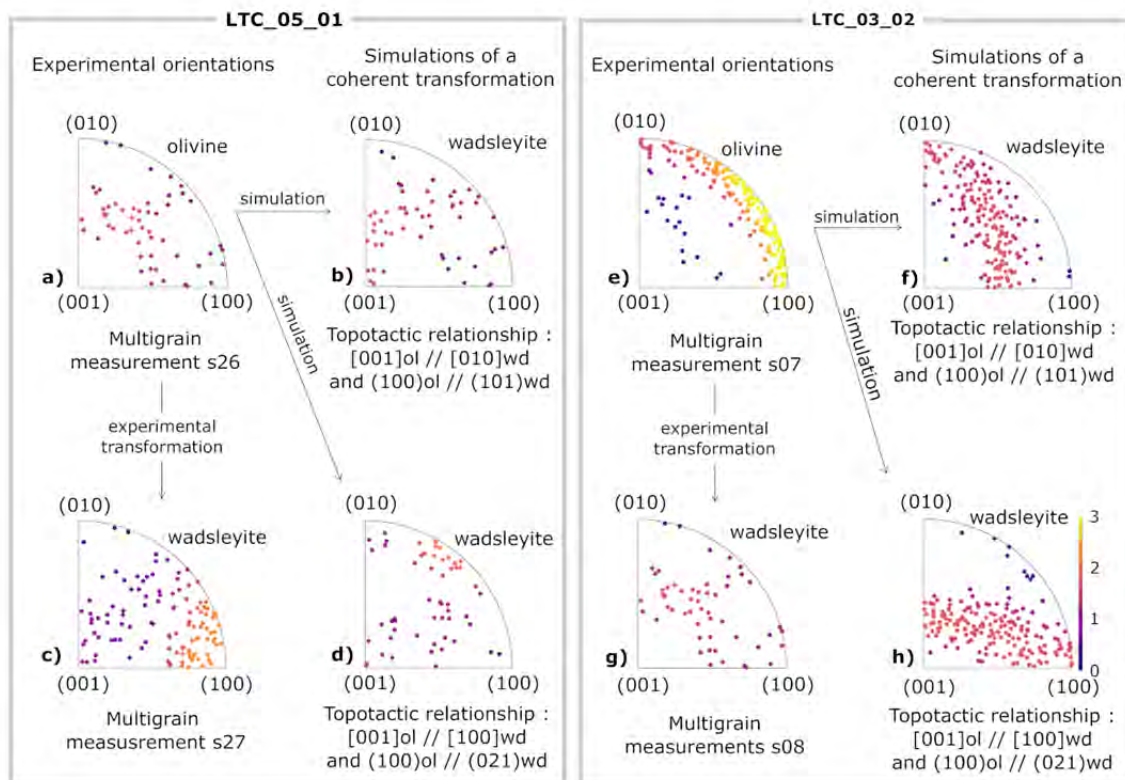
Figure 7: Coherent transformation simulations (b, d, f, h) and comparison with the experimental results (a, c, e, g), for experiments LTC_05_01 (a, b, c, d) and LTC_03_02 (e, f, g, h). For each experiment, the olivine grain orientations before transformation (a, e) are used to compute the daughter wadsleyite orientations. The computation is based on the two topotactic relationships given by Smyth et al. (2012), indicated below the corresponding inverse pole figures. c) and g) are experimental wadsleyite grains orientations just after the transformation.